Article

Asymmetric transformation of achiral gold nanoclusters with negative nonlinear dependence between chiroptical activity and enantiomeric excess

Chang Liu[1,2], Yan Zhao[1,2], Tai-Song Zhang[1], Cheng-Bo Tao[1], Wenwen Fei[1], Sheng Zhang ®[1] & Man-Bo Li ®[1] ✉

The investigation of chirality at the nanoscale is important to bridge the gap between molecular and macroscopic chirality. Atomically precise metal nanoclusters provide an ideal platform for this research, while their enantiopure preparation poses a challenge. Here, we describe an efficient approach to enantiopure metal nanoclusters via asymmetric transformation, that is, achiral $Au_{23}(SC_6H_{11})_{16}$ nanoclusters are converted into chiral and enantiopure $Au_{24}(L)_2(SC_6H_{11})_{16}$ nanoclusters by a chiral inducer phosphoramidite (L). Two enantiomers of $Au_{24}(L)_2(SC_6H_{11})_{16}$ are obtained and the crystal structures reveal their hierarchical chirality, which originates from the two introduced chiral L molecules, the transformation-triggered asymmetric rearrangement of the staple motifs on the surface of the gold core, and the helical arrangement of nanocluster molecules. The construction of this type of enantiomerically pure nanoclusters is achieved based on the easy-to-synthesize and modular L. Lastly, the chirality-related chiroptical performance was investigated, revealing a negative nonlinear CD-ee dependence.

Chirality is a fundamental characteristic in nature and can be found at various scales, from small organic molecules to macroscopic materials[1–4]. The same component materials with different chiroptical activities show distinct performance[5]. As a typical example, the S and R enantiomers of organic molecules with asymmetric sp^3 carbons display different even completely opposite biological activities[6]. That is why the asymmetric synthesis is so important in medicinal chemistry. Based on the analysis of small organic molecules' structures, we can clarify the origin of their chirality and achieve efficient enantiomer synthesis. However, when the scale of materials comes to nanometers or even micrometers (e.g., organic ligand-protected metal nanoparticles), things become complex[7–10]. The chirality of nanoparticles can originate from the chiral organic ligands, the asymmetric arrangements of metal atoms or metal-ligand motifs, as well as the

particles' asymmetric packing at a higher scale[11,12]. The complex chirality and the undefined structure of nanoparticles make the determination of chirality origin, the achievement of enantiopure isomers, and the investigation of the related performance challenging.

The atomically precise metal nanocluster constitutes an ideal platform for the research of complex systems' chirality at atomic level[13]. Moreover, chiral metal nanoclusters show unique properties and potential applications in catalysis, sensing, as well as biomedicine[14,15]. Thus, the investigation of the chirality of metal nanoclusters has received tremendous attention[16–20]. In spite of the significant progress, the achievement of enantiopure metal nanoclusters is desired but remains a great challenge. Based on the previous reports, some methods were developed for acquiring metal nanoclusters with enantiomeric excess. These methods include: (1)

enantioseparation of racemic mixtures of metal nanoclusters by chiral high-performance liquid chromatography (HPLC)[21–24] or resolving agents;[25–27] (2) enantioselective phase transfer of chiral nanoclusters;[28,29] (3) direct synthesis of enantiopure nanoclusters by using chiral organic ligands as the precursors[30–37]. However, the method for transforming an achiral metal nanocluster into a chiral one is limited. There are a few reports on the chiral ligand exchange of achiral metal nanoclusters[38,39], in which the chirality generally comes from the chiral ligands on the surface. In view of hundreds of achiral metal nanoclusters being reported[13] and the wide application of asymmetric organic transformations in pharmaceutical synthesis and industry chemistry[40,41], we envisioned the possibility of using a chiral inducer to realize the asymmetric transformation of achiral metal nanoclusters. This strategy would be developed into a general protocol for the construction of enantiopure metal nanoclusters.

We have a long-standing interest in the chirality transfer of organic molecules[42–45] as well as the construction of functional metal nanoclusters[46,47]. We developed a surface phosphorization method[48] and realized the structural evolution of thiolate-protected gold nanoclusters, which has been proven to be effective to modify the nanoclusters' structure and performance[48,49]. Inspired by these achievements, in this work, we realized the asymmetric transformation of an achiral gold nanocluster by using an easily synthesized and modular phosphine inducer. The transformation is enantiodivergent and the two optical pure enantiomers of the as-transformed nanoclusters can be obtained respectively. More interestingly, this strategy not only introduces the chirality of the phosphine inducer but also triggers the asymmetric arrangement of -S-Au-S- and -S-Au-S-Au-S- staple motifs that were originally symmetric on the surface of the gold nanocluster. An intriguing helical arrangement of nanocluster molecules was also discovered. Thus, the asymmetric transformation leads to a hierarchically chiral structure of the gold nanocluster.

Results

Asymmetric transformation process

A facilely synthesized $Au_{23}(SC_6H_{11})_{16}$ (abbreviated as Au_{23}) was used as the model nanocluster for the investigation. It is an achiral gold nanocluster, bearing an Au_{13} kernel with symmetrically arranged two -S-Au-S-Au-S-Au-S- and four -S-Au-S- staple motifs on the surface[50]. Meanwhile, it is a representative thiolate-protected gold nanocluster, which has been applied as a typical example for the studies of

structural anatomy, metal doping, and structure-property correlation[51–53]. We initiated our studies by screening different kinds of chiral phosphine ligands to react with Au_{23} (Supplementary Table 1). Butane-2,3-diybis(diphenylphosphine) with two chiral sp^3 carbons was reactive to Au_{23} but showed poor selectivity and resulted in wide product distribution (Supplementary Fig. 1a). Axially chiral 2,2′-bis(diphenylphosphino)−1,1′-binaphthyl (BINAP) with sterically hindered phosphine sites displayed low activity to Au_{23} instead, and led to the recovery of the starting materials (Supplementary Fig. 1b). Chiral phosphoric acid resulted in the decomposition of Au_{23}, probably due to its strong acidity. Delightedly, a "privileged" ligand phosphoramidite[48] was found to demonstrate satisfactory reactivity as well as good selectivity (Supplementary Fig. 2). This ligand was first introduced by Feringa and coworkers[54,55] and Alexakis and coworkers[56] in the late 1990s for copper-catalyzed asymmetric conjugate additions. They are modular, easy to synthesize, and widely applied as a versatile and readily accessible class of chiral ligands in asymmetric catalysis[56]. Racemic phosphoramidite with a diethylamine module (Rac)-L_1 was prepared initially to react with Au_{23} at room temperature (Fig. 1a). This reaction is efficient, giving an exclusive nanocluster product in high yield. The obtained nanocluster showed a different polarity to Au_{23} based on the preparative thin layer chromatography (PTLC), demonstrating that a different nanocluster (LC_1) was formed (Supplementary Fig. 2). Meanwhile, the ultraviolet and visible (UV-vis) spectrum of LC_1 is quite similar to that of Au_{23}, and only a slight blueshift of the characteristic peaks at 460 and 575 nm was observed during the transformation (Fig. 1b). This result suggests that the structure of LC_1 would be relevant to that of Au_{23}. (R)-L_1 and (S)-L_1 reacted with Au_{23}, affording (R)-LC_1 and (S)-LC_1 with the same UV-vis spectra (Fig. 1b). Electrospray ionization mass spectrometry (ESI-MS) was used to determine the composition of the as-obtained nanocluster. A single peak at $m/z = 3806.15$ was observed on the positive mode with the addition of CsOAc. This peak is assigned to $[Au_{24}(L_1)_2(SC_6H_{11})_{16} + 2Cs]^{2+}$ (Fig. 1c), and the experimental isotope patterns match very well with the calculated one (Fig. 1c, inset). The ESI-MS result suggests that the as-obtained nanocluster is charge-neutral and determines the molecular formula of LC_1 to be $Au_{24}(L_1)_2(SC_6H_{11})_{16}$.

Crystal structures analysis

Single crystals of (R)-LC_1 and (S)-LC_1 were obtained in the mixed solvents of dichloromethane and hexane. From the crystal
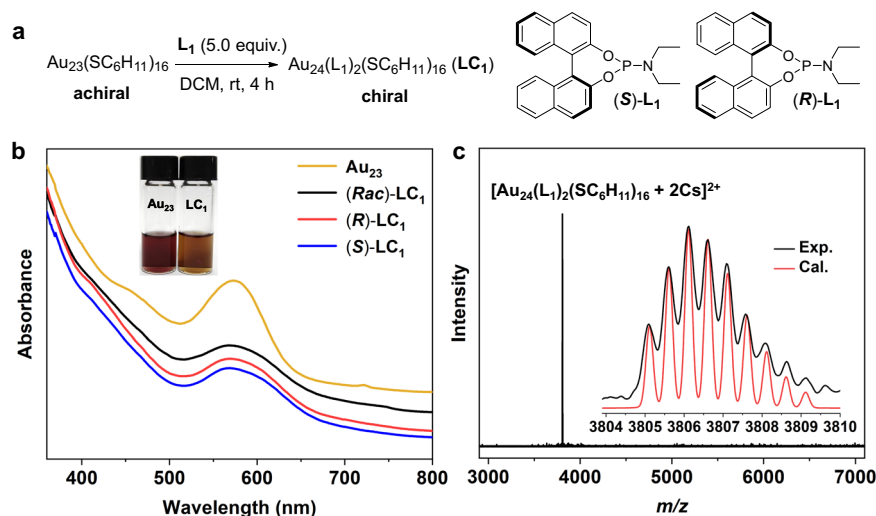

Fig. 1 | Procedure and characterizations of asymmetric transformation.
a Procedure of the asymmetric transformation. **b** UV-vis spectra of Au_{23} (yellow trace), (Rac)-LC_1 (black trace), (R)-LC_1 (red trace) and (S)-LC_1 (blue trace). Inset: the photographs of Au_{23} and LC_1 in DCM. **c** ESI-MS spectrum of LC_1. Inset: the experimental (black trace) and calculated (red trace) isotope patterns. Source data are provided as a Source Data file.
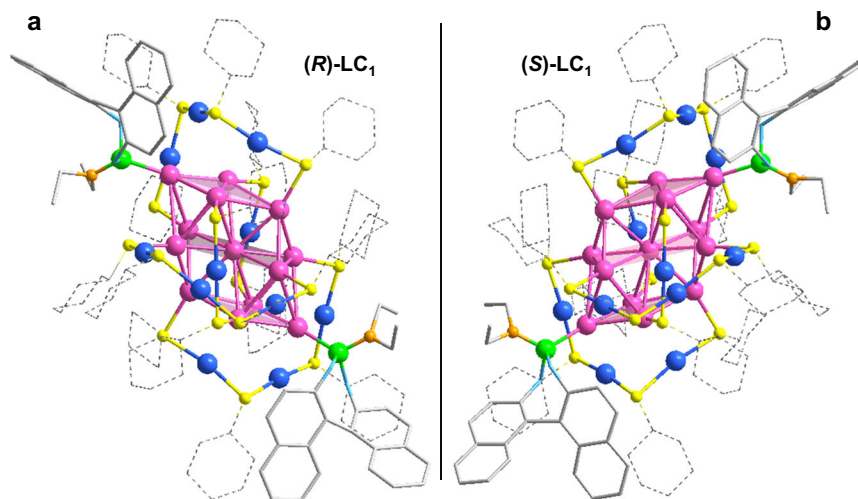
Fig. 2 | Crystal structures. a Structure of (***R***)-**LC₁**. **b** Structure of (***S***)-**LC₁**. Color label: Au = pink, blue; S = yellow; P = green; N = orange; O = light blue; C = gray. H atoms are omitted for clarity.
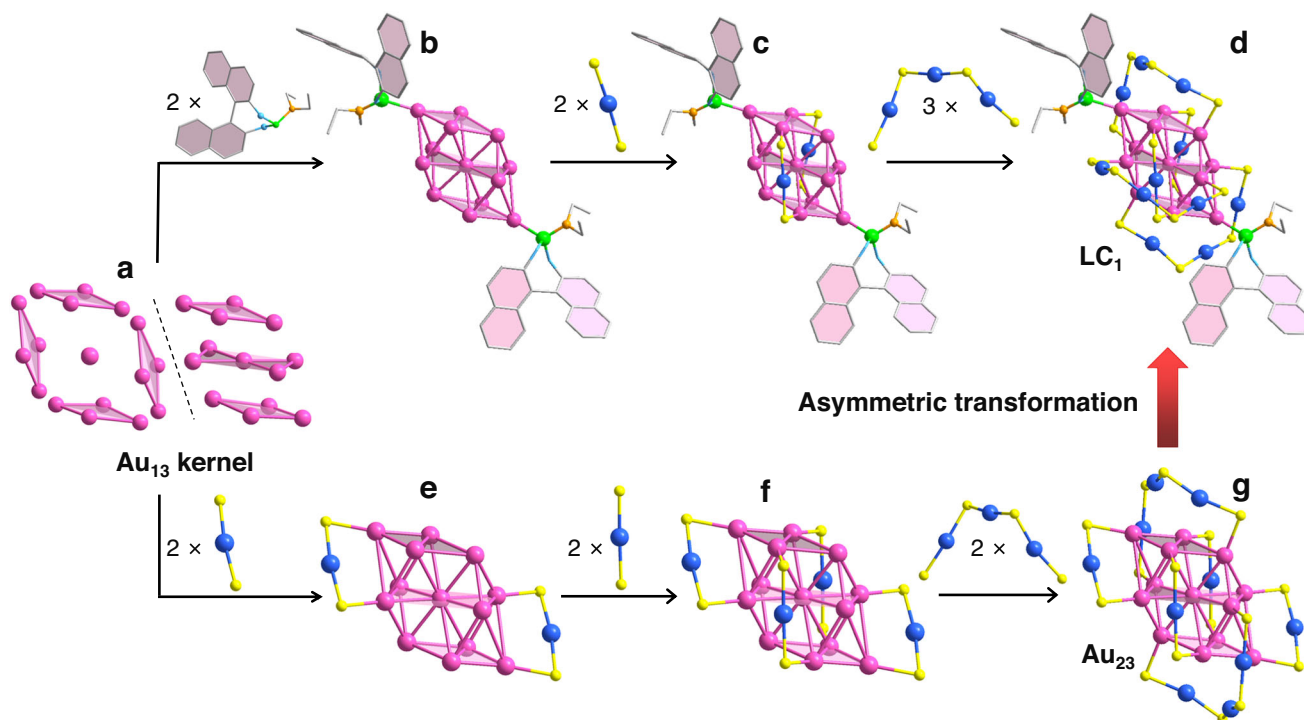
Fig. 3 | Structural anatomy of LC₁ and Au₂₃. a The Au₁₃ kernel. **b** Au₁₃ kernel with two phosphoramidites **L₁**. **c** Au₁₃ kernel with two phosphoramidites **L₁** and two -S-Au-S- motifs. **d** The total structure of **LC₁**. **e** Au₁₃ kernel with two -S-Au-S- motifs. **f** Au₁₃ kernel with four -S-Au-S- motifs. **g** The total structure of Au₂₃. Color label: Au = pink, blue; S = yellow; P = green; N = orange; O = light blue; C = gray. H atoms are omitted for clarity.

structures revealed by single-crystal X-ray diffraction (SCXRD), (***R***)-**LC₁** and (***S***)-**LC₁** all crystallized in the enantiomorphic P2₁ space group, which is different from the centrosymmetric Ccca space group of Au₂₃[44]. The (***R***)-**LC₁** and (***S***)-**LC₁** nanocluster molecules take a similar 'ABCD' stacking sequence along the [100], [010] and [001] directions based on the observation of their crystallographic arrangements (Supplementary Figs. 4 and 5). The total structures of (***R***)-**LC₁** and (***S***)-**LC₁** demonstrate that the as-transformed nanoclusters are composed of 24 gold atoms, 16 cyclohexanethiols, and two phosphoramidites **L₁** (Fig. 2), which is consistent with the molecular formula revealed by ESI-MS. (***R***)-**LC₁** and (***S***)-**LC₁** cannot overlap with each other, and show near-perfect mirror images (Fig. 2), indicating

that the (***R***)- and (***S***)-phosphoramidite-induced transformations of achiral Au₂₃ leads to a pair of enantiomeric nanoclusters.

One of the enantiomers (***R***)-**LC₁** was selected as an example for further structural anatomy. As shown in Fig. 3, **LC₁** consists of an Au₁₃ kernel, which can be seen as an Au₄-Au₅-Au₄ sandwich structure, and also a central gold atom surrounded by four common-vertex rhombic blocks (Fig. 3a). The central gold atom is associated with the surrounded ten gold atoms with the average Au–Au bond of 2.84 Å (Supplementary Fig. 6) except for the two gold atoms on the vertices (which are far away from the central gold atom with the distances of 4.28 and 4.30 Å). The two vertices are coordinated with the phosphine sites of phosphoramidites **L₁** (Fig. 3b), and the other ten gold atoms are
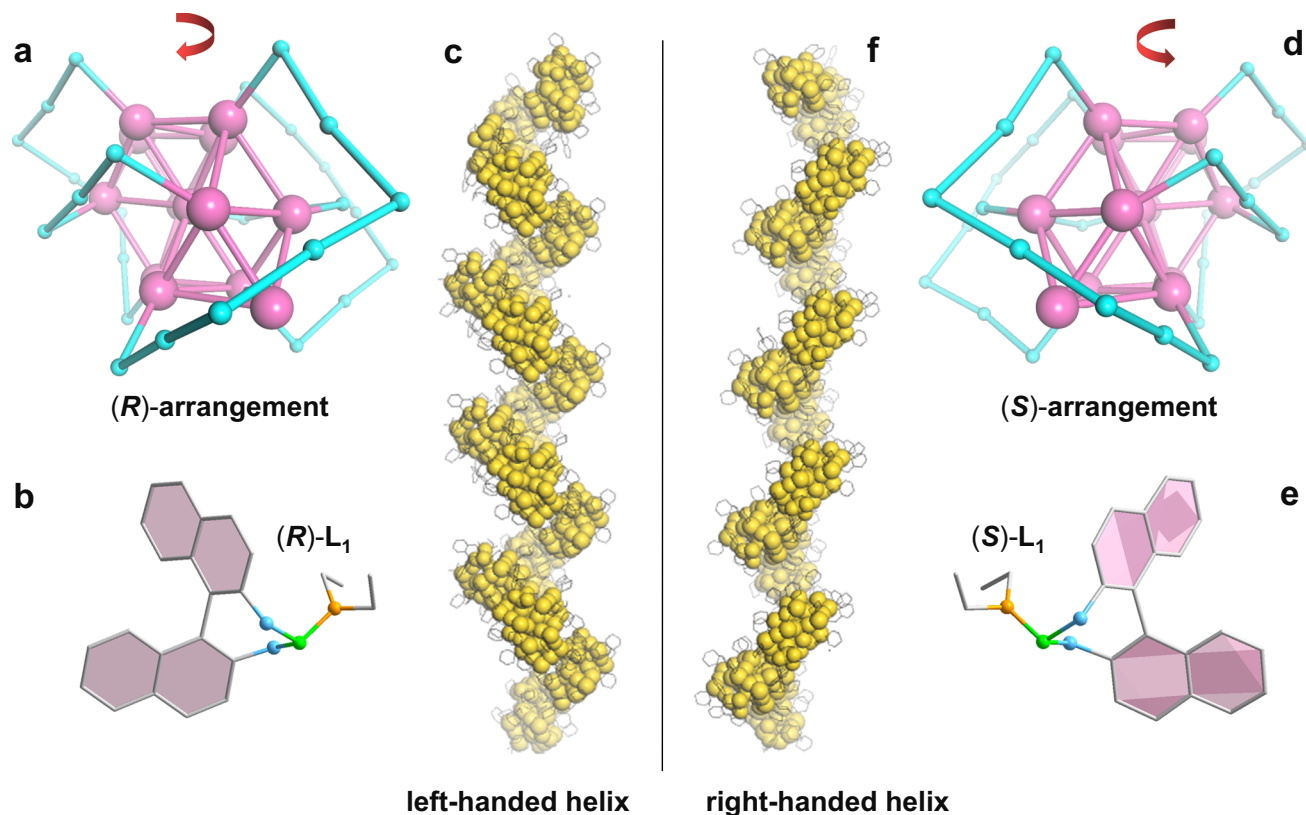
Fig. 4 | Representation of hierarchically chiral structures of (R)-LC$_1$ and (S)-LC$_1$.
a, **d** The asymmetric arrangement of -S-Au-S- and -S-Au-S-Au-S-Au-S- motifs on the surface of the Au$_{13}$ kernel. **b**, **e** The intrinsic chirality of phosphoramidite ligand at the two vertices of the Au$_{13}$ kernel. **c**, **f** The helical arrangement of nanocluster molecules. Color label: Au$_{13}$ kernel = rose red; -S-Au-S- and -S-Au-S-Au-S-Au-S- staple motifs = cyan; Helical nanocluster molecules = yellow; P = green; N = orange; O = light blue; C = gray. H atoms are omitted for clarity.

covered by two -S-Au-S- and three -S-Au-S-Au-S-Au-S- staple motifs (Fig. 3c, d). Notably, **LC$_1$** and Au$_{23}$ nanoclusters have similar sandwich Au$_{13}$ kernels. A careful comparison of the Au–Au distances on the upper and lower Au$_4$ layers reveals that the Au$_{13}$ kernel in Au$_{23}$ is completely centrosymmetric (Supplementary Fig. 7a). The analysis of Au–Au distances between the Au$_4$ and Au$_5$ layers further confirms this conclusion (Supplementary Fig. 7b). The examination of the Au$_4$-Au$_5$-Au$_4$ sandwich kernel of **LC$_1$** indicates that its Au$_{13}$ kernel is slightly twisted (Supplementary Fig. 7c, d). Despite the tiny distortion of the Au$_{13}$ kernel in **LC$_1$**, the main difference between **LC$_1$** and Au$_{23}$ comes from the introduced phosphoramidites (**L$_1$**) ligands and the arrangements of -S-Au-S- and -S-Au-S-Au-S-Au-S- motifs on the surface of the Au$_{13}$ kernel. Specifically, Au$_{23}$ has four -S-Au-S- and two -S-Au-S-Au-S-Au-S- staple motifs (Fig. 3e–g), in which two of the -S-Au-S- motifs take the same arrangement as that in **LC$_1$**, bridging the upper and lower Au$_4$ layers of the Au$_4$-Au$_5$-Au$_4$ sandwich kernel (Fig. 3c, f). The other two -S-Au-S- and all of the -S-Au-S-Au-S-Au-S- motifs of Au$_{23}$ locate between the layers of the middle Au$_5$ and the upper (or lower) Au$_4$ (Fig. 3e, g). The total six staple motifs on the surface of the Au$_{13}$ kernel are also completely centrosymmetric in Au$_{23}$ (Fig. 3g). In contrast, the arrangement of -S-Au-S-Au-S-Au-S- motifs in **LC$_1$** is more diversified. One of the -S-Au-S-Au-S-Au-S- motifs twists around the middle Au$_5$ layer, and the other two locate between the middle Au$_5$ layer and the (upper or lower) Au$_4$ layer (Fig. 3d).

Asymmetric transformation mechanism
Based on the experimental results and crystal structures of **LC$_1$** and Au$_{23}$, a proposed transformation mechanism from Au$_{23}$ to **LC$_1$** was shown in Supplementary Fig. 8. The two vertex Au atoms of the sandwich Au$_{13}$ kernel of Au$_{23}$ constitute two open sites (Supplementary Fig. 8a), which are easily attacked by the phosphine site of ligand **L$_1$**.

The Au–P interaction would trigger the cleavage of Au–S bonds and the further dissociation of the two corresponding -S-Au-S- staple motifs (Supplementary Fig. 8b). A subsequential rearrangement of a -S-Au-S-Au-S-Au-S- motif (Supplementary Fig. 8c) and the association of the two vacant Au sites with another -S-Au-S-Au-S-Au-S- would generate asymmetrically arranged staple motifs on the Au$_{13}$ kernel and give **LC$_1$** (Supplementary Fig. 8d). During the transformation, the Au$_{13}$ kernel is retained and only slightly twisted, while two short -S-Au-S- staple motifs are replaced by two phosphine ligands **L$_1$** and a long -S-Au-S-Au-S-Au-S- staple motifs. Therefore, **LC$_1$** contains one more Au atom and two **L$_1$** while possessing the same number of thiol ligands, when compared to Au$_{23}$. We carefully analyzed the product components of the reaction between Au$_{23}$ and **L$_1$** (Supplementary Table 2). Apart from a few undesired complexes and nanoparticles, **LC$_1$** was isolated as the major product with a yield of 65% (based on the Au atom). According to the whole process proposed in Supplementary Fig. 8, the mole ratio of the Au atom of two decomposed -S-Au-S- and one generated -S-Au-S-Au-S-Au-S- is 2/3, which is basically consistent with the yield (65%) of **LC$_1$** observed. This result suggests that 3 equivalents of Au$_{23}$ would produce 2 equivalents of **LC$_1$**, and the additional Au atom of **LC$_1$** probably comes from the decomposed -S-Au-S- staple motifs of Au$_{23}$. The Au$_{23}$ that are not transformed into **LC$_1$** during the reaction would decompose or aggregate into complexes or nanoparticles.

Hierarchical chirality
Further analysis of the two enantiomers' structures reveals the origin of the chirality of the **LC$_1$** nanocluster (Fig. 4). First, (R)-**LC$_1$** and (S)-**LC$_1$** bear the same Au$_{13}$ kernel that can overlap completely (Supplementary Fig. 9), demonstrating that the Au$_{13}$ kernel is achiral. Second, the two short -S-Au-S- and three long -S-Au-S-Au-S-Au-S- motifs that surround
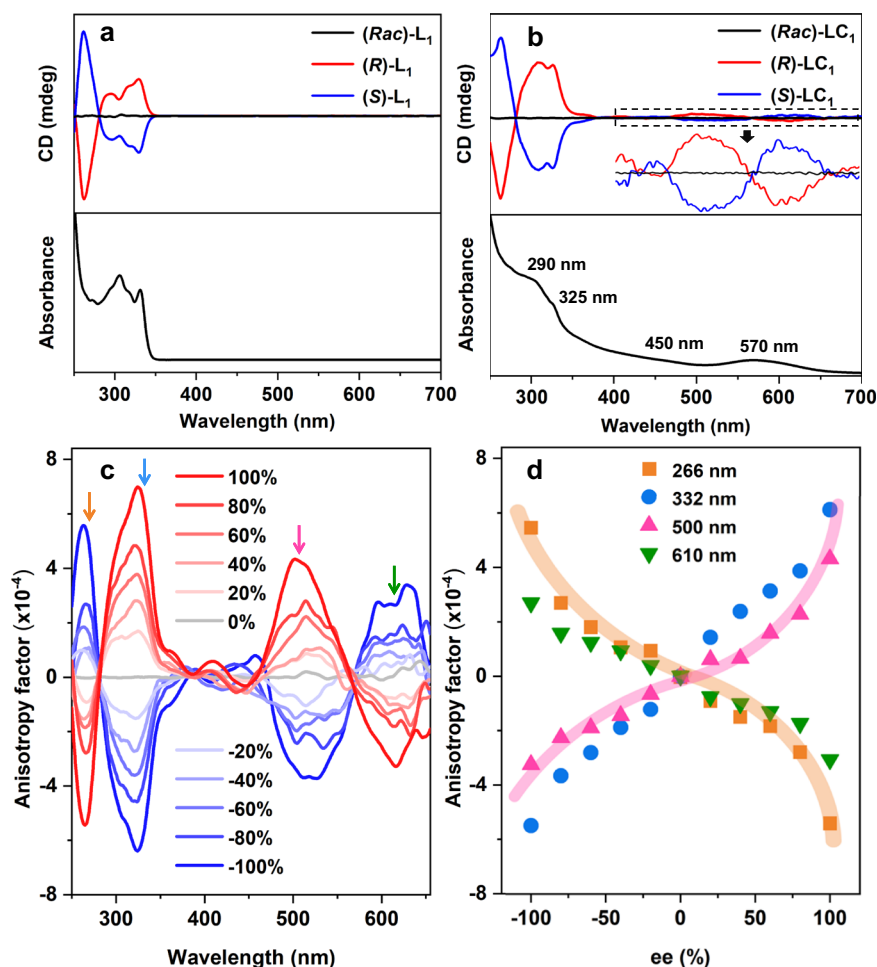
Fig. 5 | Negative nonlinear dependence between chiroptical activity and enantiomeric excess. a Combined CD-absorption spectra of (*Rac*)-L$_1$ (black trace), (*R*)-L$_1$ (red trace) and (*S*)-L$_1$ (blue trace). **b** Combined CD-absorption spectra of (*Rac*)-LC$_1$ (black trace), (*R*)-LC$_1$ (red trace) and (*S*)-LC$_1$ (blue trace). Inset: the enlarged view from 400 to 700 nm, and the magnification factor is 5. **c** Anisotropy factors of LC$_1$ prepared by different ee values of L$_1$. **d** The negative nonlinear CD-ee dependence between the chiroptical activity of LC$_1$ and enantiomeric excess of L$_1$ based on anisotropy. The solid and broader highlighted colored lines in (**d**) are merely guides to the eye. Source data are provided as a Source Data file.

around the sandwich Au$_{13}$ kernel of (*R*)-LC$_1$ cannot overlap with that of (*S*)-LC$_1$. Moreover, the arrangements of these motifs in (*R*)-LC$_1$ and (*S*)-LC$_1$ are completely mirror-symmetric (Fig. 4a, d), indicating that the chirality of LC$_1$ partially comes from the enantiotropic arrangement (tentatively defined as (*R*)- and (*S*)-arrangements) of surface motifs. Third, the (*R*)-L$_1$ and (*S*)-L$_1$ at the vertices of the Au$_{13}$ kernels of (*R*)-LC$_1$ and (*S*)-LC$_1$ are enantiomeric (Fig. 4b, e), which also contribute to the chirality of the nanocluster. More interestingly, we found that *R*)-LC$_1$ and (*S*)-LC$_1$ nanocluster molecules take the left-handed helix and right-handed helix arrangements, respectively, based on the observation of the crystallographic arrangements of the two enantiomeric nanoclusters (Supplementary Fig. 10). One of the helical and enantiotropic chains of (*R*)-LC$_1$ and (*S*)-LC$_1$ molecular arrangements were picked out and shown in Fig. 4c, f. The intermolecular hydrogen bonds might play an important role in the helical arrangement of nanocluster molecules (Supplementary Fig. 11). Based on the above analysis, LC$_1$ demonstrates a hierarchically chiral structure, which originates from three aspects: (1) the asymmetric arrangement of the -S-Au-S- and -S-Au-S-Au-S-Au-S- motifs on the surface of the Au$_{13}$ kernel; (2) the intrinsic chirality of phosphoramidite ligand at the two vertices of the Au$_{13}$ kernel; (3) the helical arrangement of nanocluster molecules. Thus, the phosphoramidite-induced asymmetric transformation from Au$_{23}$ to LC$_1$ not only introduces the intrinsic chirality of phosphoramidite itself

but also triggers the asymmetric rearrangements of the staple motifs and nanocluster molecules that were originally symmetric in Au$_{23}$.

Negative nonlinear CD-ee dependence

The asymmetric transformation process is enantiodivergent, and the as-obtained (*R*)-LC$_1$ and (*S*)-LC$_1$ are enantiopure, displaying nearly perfect mirror-symmetric circular dichroism (CD) signals from 250 to 700 nm. Specifically, (*R*)-LC$_1$ gave positive Cotton effects at 310, 328, 405 and 500 nm with negative Cotton effects at 260, 425 and 600 nm, while (*S*)-LC$_1$ demonstrated the completely opposite Cotton effects (Fig. 5b). Based on the combined CD-absorption spectra, the zero-crossing points at 450 and 570 nm in the CD spectrum are consistent with the characteristic absorptions in the UV-vis spectrum, indicating that the exciton coupling happens. Compared with the chiral inducer (*R*)-L$_1$ and (*S*)-L$_1$ that only showed simple CD signals from 250 to 350 nm (Fig. 5a), the CD spectra of (*R*)-LC$_1$ and (*S*)-LC$_1$ displayed much more abundant signals. The anisotropy factors ($g = \Delta Abs/Abs$) of (*R*)-L$_1$ and (*S*)-L$_1$ were calculated in the wavelength ranging from 250 to 700 nm (Fig. 5c), showing a maximum value (g_{max}) of 0.75×10^{-3} at 328 nm.

To gain a deeper insight into the asymmetric transformation of Au$_{23}$ induced by phosphoramidite, the relationship between the chiroptical activity of nanocluster LC$_1$ and the enantiomeric excess (ee) of

inducer L_1 was investigated. As shown in Fig. 5c, with the increment of ee values of L_1, the anisotropy of LC_1 increase accordingly. However, the CD-ee dependence is not linear based on the data collected at 266, 332, 500, and 610 nm of the anisotropy factors. Interestingly, we tried to obtain clusters containing one (*R*)-L_1 and one (*S*)-L_1 in the ligand shell by the reaction of Au_{23} with (*Rac*)-L_1 (ee = 0%). However, the crystals suitable for single-crystal X-ray diffraction test were determined to be either (*R*)-LC_1 or (*S*)-LC_1. Considering that (*Rac*)-LC_1 showed none of the CD signal (Fig. 5b), the racemic clusters are likely composed of equimolar (*R*)-LC_1 and (*S*)-LC_1. This result is consistent with the nonlinear CD-ee dependence and suggests that the clusters with one (*R*)-L_1 and one (*S*)-L_1 in the ligand shell are thermodynamically unfavorable products. Notably, because other chiral nanoclusters than LC_1 exist in the crude product (Supplementary Table 2), the LC_1 nanocluster showed slightly different CD spectra from that of the crude product which was directly obtained from the reaction of Au_{23} and L_1 (Supplementary Fig. 14). This might make the should-be linear CD-ee dependence change into nonlinear one. As we know, there are three types of CD-ee dependence for the chiral auxiliaries-induced chirality of materials: linear, positive nonlinear, and negative nonlinear[57]. The linear CD-ee dependence is quite common, and the positive nonlinear CD-ee dependence (also known as "majority rules effect") representing the chiral amplification phenomenon has only been found in a minority of the cases. In sharp contrast, the negative nonlinear CD-ee dependence has been much less reported. Herein, this dependence was found in metal nanoclusters. The CD-ee dependence of the asymmetric transformation process is nonlinear, indicating that more than one chiral auxiliary is involved in the intermediate of the asymmetric transformation of Au_{23}, providing support for the proposed mechanism (Supplementary Fig. 8). The negative nonlinear CD-ee dependence secures a steeper slope at the ee region close to 100%, which would be applied in the future for the accurate determination of enantiopurity of molecules at the high ee region[58]. Such determination is important in practical applications, such as the optimization of asymmetric catalyst performance.

Asymmetric transformation application

Apart from the introduction of hierarchical chirality, the phosphoramidite-induced transformation of Au_{23} also leads to the improvement of stability and photoluminescence of the gold nanocluster. Time-dependent UV-vis spectra showed that LC_1 was stable even at 80 °C under the ambient atmosphere (Supplementary Fig. 15b). In contrast, Au_{23} was quickly decomposed under the same conditions (Supplementary Fig. 15a). Based on the molecular formula $(Au_{24}(L_1)_2(SC_6H_{11})_{16})$ of LC_1, it bears an eight-electron closed-shell $(24 \times 1 - 16 \times 1 = 8)$ structure. Moreover, differential pulse voltammetry (dpv) reveals that the oxidation (0.22 V) and reduction (−1.65 V) barriers of LC_1 are higher than that of Au_{23} (0.07 V and −1.34 V, Supplementary Fig. 16). The stable electronic structure and the relatively large electrochemical gap all contribute to the high stability of LC_1. The fluorescence emission peaks of Au_{23} and LC_1 locate at a similar wavelength of 720 nm based on the photoluminescence spectra (Supplementary Fig. 17). However, the emission intensity of LC_1 is almost five times higher than that of Au_{23}. LC_1 dissolved in DCM displayed stronger red emission than Au_{23} by keeping their concentrations the same (Supplementary Fig. 17, inset). Considering that LC_1 and Au_{23} bear the basically same Au_{13} kernel, the fluorescence enhancement probably originates from the asymmetric transformation-resulted structural modification on the surface.

As mentioned above, phosphoramidite is modular and easy to synthesize. Using different amino modules involving sterically hindered, unsymmetric, aryl and alkyl groups, we synthesized the other four enantiopure phosphoramidites (L_{2-5}), which were applied to induce the asymmetric transformations of Au_{23}. These phosphoramidites all reacted well with Au_{23}, affording LC_{2-5} with racemic, R and

S configurations (Fig. 6). The exciton-coupled CD profiles with respect to the UV-vis spectra of LC_1-LC_5 were carefully analyzed. Based on the combined CD-absorption spectra (Supplementary Fig. 12a–e), LC_1, LC_2, LC_3 and LC_5 demonstrate characteristic absorptions at 290, 325 and 570 nm, and a weak peak at about 450 nm. Accordingly, these four clusters showed consistent zero-crossing points at 450 and 570 nm in the CD profiles. LC_4 showed a slightly different CD spectrum. This can be explained by a different UV-vis spectrum of ligand L_4, compared to that of the other four phosphoramidite ligands (Supplementary Fig. 12f). The distinctive absorption of L_4 might originate from the conjugated π system of the two phenyl groups on the nitrogen atom. The UV-vis spectrum of LC_4 demonstrates a stronger absorption peak at 410 nm and a bathochromic shift at 580 nm, which are also slightly different from that of LC_1, LC_2, LC_3 and LC_5. The absorption at 410 nm is consistent with an obvious Cotton effect at this wavelength. ESI-MS spectra of these nanoclusters confirmed their molecular formulas to be $Au_{24}(L_{2-5})_2(SC_6H_{11})_{16}$ (Fig. 6a–d). The above analysis combined with the ESI-MS spectra suggest that LC_1-LC_5 have similar structures.

Discussion

In summary, we realized the asymmetric transformation of an achiral metal nanocluster in this work for the achievement of enantiopure metal nanoclusters. Phosphoramidites (**L**) were developed as efficient chiral auxiliaries to induce the enantiodivergent processes, and the enantiomeric nanoclusters (*R*)- and (*S*)-$Au_{24}(L)_2(SC_6H_{11})_{16}$ were synthesized separately from achiral Au_{23}. Structural analysis reveals that the asymmetric transformation not only brings the intrinsic chirality of phosphoramidite but also triggers the asymmetric rearrangement of the staple motifs and nanocluster molecules that were originally symmetric in Au_{23}, constituting the hierarchical chirality of $Au_{24}(L)_2(SC_6H_{11})_{16}$. A negative nonlinear CD-ee dependence was found for the relationship between the chiroptical activity of $Au_{24}(L)_2(SC_6H_{11})_{16}$ and the enantiomeric excess of **L**. The phosphoramidite is modular and a series of substituents can be introduced, leading to the functional diversity of the as-transformed chiral nanoclusters. We expect that our work will stimulate further research on the construction of enantiopure metal nanoclusters and the chirality of complex systems.

Methods

Characterizations

ESI-MS were acquired on a Waters Q-TOF mass spectrometer equipped with a Z-spray source. All UV-vis absorption measurements were performed on a SPECORD 210 PLUS spectrophotometer. SCXRD data were measured by using a Stoe Stadivari diffractometer. The structures were solved and refined using the SHELXT software. CD spectra were obtained by Circular chromatograph J-1700, and the reference solvent for measurement is DCM. Fluorescence spectra were obtained by a spectrofluorometer FS 5. Electrochemical measurements were performed with a CHI770E electrochemistry workstation in a three-electrode system using an Ag/AgCl electrode as the reference electrode, a glassy carbon electrode as the working electrode and a platinum wire electrode as the auxiliary electrode. NMR spectra were recorded at 400 MHz. Chemical shifts (δ) are reported in ppm, using the residual solvent peak in CDCl₃ (7.26 ppm) as the internal standard. Coupling constants (*J*) are given in Hz.

Synthesis of Au₂₃

HAuCl₄·3H₂O (0.3 mmol, 118 mg) and tetraoctylammonium bromide (TOAB, 0.35 mmol, 190 mg) were dissolved in methanol (15 mL) in a 100 mL round-bottom flask. After vigorously stirring for 15 min, cyclohexanethiol (1.6 mmol, 196 μL) was added to the mixture at room temperature. After 15 min, NaBH₄ (3 mmol, 114 mg dissolved in 6 mL of cold Nanopure water) was rapidly added to the solution under
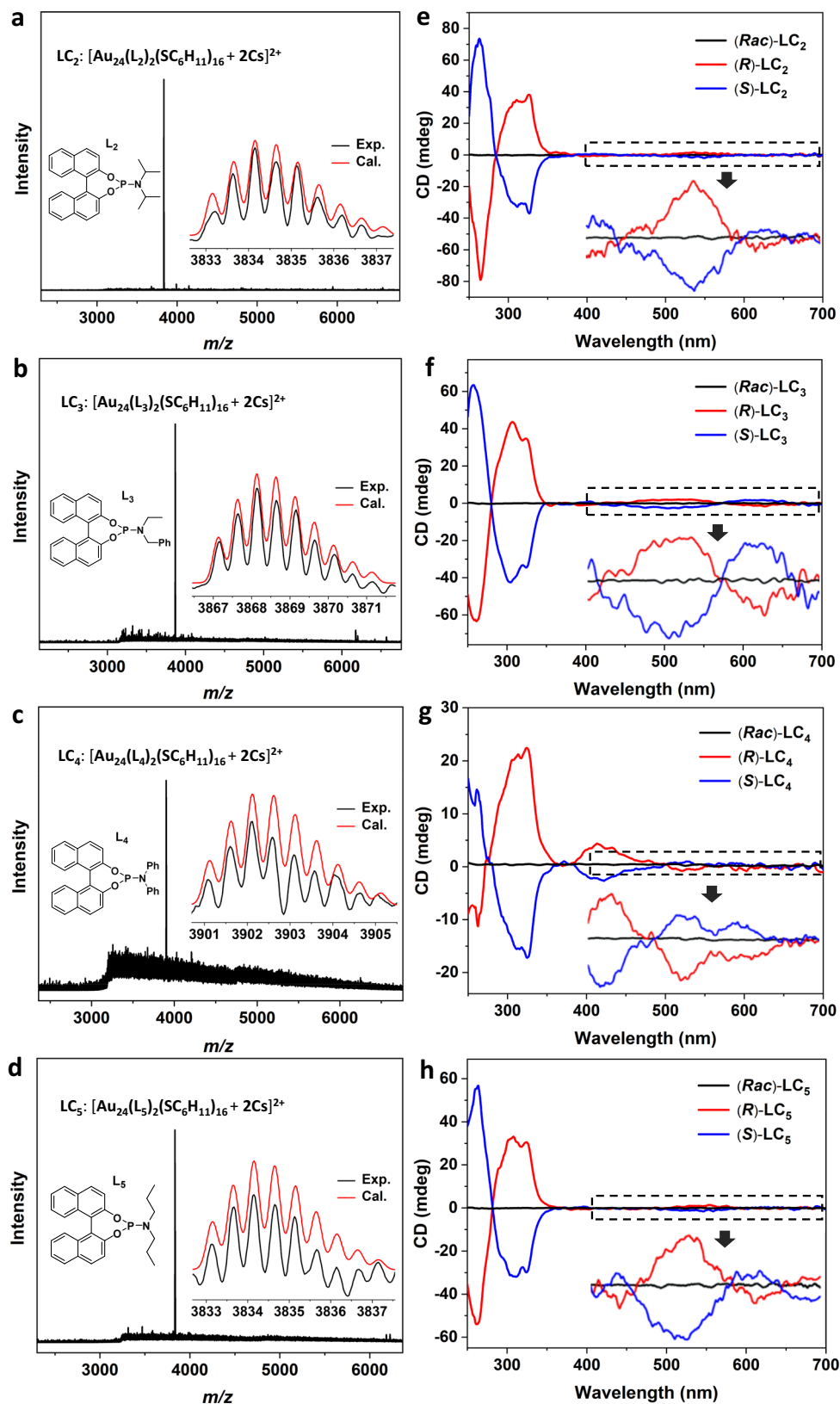
Fig. 6 | Characterizations of LC$_{2-5}$. a–d ESI-MS spectra of **LC$_{2-5}$**. Inset: the structures of **L$_{2-5}$**, and the experimental (black trace) and calculated (red trace) isotope patterns of **LC$_{2-5}$. e–h** CD spectra of (***Rac***)- (black trace), (***R***)- (red trace), and (***S***)-**LC$_{2-5}$** (blue trace). Inset: the enlarged view of CD spectra from 400 to 700 nm, the magnification factors of **LC$_{2-5}$** are 5, 4, 3 and 6. Source data are provided as a Source Data file.

vigorous stirring. The reaction mixture was allowed to stir overnight and finally gave Au_{23} in 20% yield (purified by recrystallization).

Preparation of phosphoramidite (L_{1-5})

By using the procedure for the preparation of (**S**)-L_1 as an example: Triethylamine (5.0 eq., 25 mmol, 3.5 mL) was added dropwise to a stirred ice-cooled solution of PCl_3 (5 mmol, 436 μL) in CH_2Cl_2 (35 mL). The ice bath was removed and the solution was warm to room temperature before diethylamine (5 mmol, 517 μL) was added. After 5 h, (**S**)-binaphthol (5 mmol, 1.43 g) was added to the suspension and the resulting mixture was left to stir for an additional 18 h. The purification of (**S**)-L_1 was achieved via column chromatography on silica gel (eluent: Pentane/EtOAc = 60/1). (**Rac**)-, (**R**)- and (**S**)-L_{1-5} were prepared following the procedure above.

Synthesis of LC_{1-5} from Au_{23}

By using the procedure for the synthesis of (**S**)-LC_1 as an example: 5.0 equivalents of (**S**)-L_1 (4.24 mg) were added into the CH_2Cl_2 (1.5 mL) solution of Au_{23} (15.0 mg). After the completion of the reaction in 4 h, the mixture was washed with MeOH for 2-3 times to give the crude product (**S**)-LC_1 (precipitate), which was recrystallized in the system of CH_2Cl_2/n-hexane. Red hexagon crystals were obtained after 7 days, which were suitable for ESI-MS, SCXRD and the other characterizations. (**Rac**)-, (**R**)- and (**S**)-LC_{1-5} were prepared following the procedure above.

CD-ee dependence studies

First, L_1 with different ee (−100%, −80%, −60%, −40%, −20%, 0%, 20%, 40%, 60%, 80% and 100%) were prepared by mixing optical pure (**R**)-L_1 and (**S**)-L_1. The amount of (**R**)-L_1 and (**S**)-L_1 used for each sample was calculated via Eq. (1) and is also shown in Supplementary Table 3. Second, 5.0 equivalents of L_1 (5.0 mg) with specific ee was added into 18.0 mg of Au_{23} (dissolved in 1.5 mL of DCM). After 4 h, the reaction was purified by column chromatography on silica gel (eluent: DCM/MeOH = 20/1) to give LC_1. Third, the purified LC_1 from the reaction of Au_{23} and L_1 with different ee was used for the CD test. The corresponding anisotropy factors (g) were obtained via Eq. (2). θ and Abs refer to ellipticity and absorbance, respectively.

$$ee = \frac{[R] - [S]}{[R] + [S]} \times 100\% \tag{1}$$

$$g = \frac{\theta \, / \, mdeg}{32{,}980 \times Abs} \tag{2}$$

Stability studies

For this, 5.0 mg of pure Au_{23} or LC_1 was dissolved in 2 mL of toluene. The solution was gently stirred at 80 °C. The time-dependent UV-vis absorption spectra were obtained based on the mixture (Supplementary Fig. 15). 5.0 mg of Au_{23} or LC_1 was dissolved in Bu_4NPF_6 (70 mg)-DCM (2 mL) solution and the electrochemical property of the nanocluster was measured using an electrochemical workstation. Before the experiment, the working electrode was polished with a mixture of Al_2O_3 and water and then cleaned sequentially with water and MeOH. The experiment was performed at an amplitude of 0.05 V, a pulse width of 0.05 s, a sampling width of 0.02 s and a pulse period of 0.1 s. The sample was always in a nitrogen atmosphere.

Photoluminescence studies

The excitation and emission spectra of Au_{23} and LC_1 were obtained by dissolving the nanocluster in DCM at room temperature. The concentration of the samples was kept at the same to be 2.3×10^{-5} M. The excitation wavelength was kept at 350 and 360 nm, respectively, for the emission spectra of Au_{23} and LC_1. The data were collected based on the same parameters.

Reporting summary

Further information on research design is available in the Nature Portfolio Reporting Summary linked to this article.

Data availability

The data that support the findings of this study are available from the corresponding author upon request. Source data are provided with this paper. The X-ray crystallographic structures reported in this work have been deposited at the Cambridge Crystallographic Data Center (CCDC) under deposition numbers 2216153 and 2216156 for (**R**)- and (**S**)-$Au_{24}(L_1)_2(SC_6H_{11})_{16}$, respectively. These data can be obtained free of charge from the CCDC via https://www.ccdc.cam.ac.uk/structures/. Source data are provided with this paper.

References

1. Zeng, C., Chen, Y., Kirschbaum, K., Lambright, K. J. & Jin, R. Emergence of hierarchical structural complexities in nanoparticles and their assembly. *Science* **354**, 1580–1584 (2016).
2. Yeom, J. et al. Chiral templating of self-assembling nanostructures by circularly polarized light. *Nat. Mater.* **14**, 66–72 (2015).
3. Che, S. et al. Synthesis and characterization of chiral mesoporous silica. *Nature* **429**, 281–284 (2004).
4. Barron, L. D. Symmetry and molecular chirality. *Chem. Soc. Rev.* **15**, 189–223 (1986).
5. Feringa, B. L., van Delden, R. A., Koumura, N. & Geertsema, E. M. Chiroptical molecular switches. *Chem. Rev.* **100**, 1789–1816 (2000).
6. Ito, T. et al. Identification of a primary target of thalidomide teratogenicity. *Nature* **327**, 1345–1350 (2010).
7. Aida, T., Meijer, E. & Stupp, S. Functional supramolecular polymers. *Science* **335**, 813–817 (2012).
8. Yashima, E. et al. Supramolecular helical systems: helical assemblies of small molecules, foldamers, and polymers with chiral amplification and their functions. *Chem. Rev.* **116**, 13752–13990 (2016).
9. Magnin, Y., Amara, H., Ducastelle, F., Loiseau, A. & Bichara, C. Entropy-driven stability of chiral single-walled carbon nanotubes. *Science* **362**, 212–215 (2018).
10. Nakagawa, M. & Kawai, T. Chirality-controlled syntheses of double-helical Au nanowires. *J. Am. Chem. Soc.* **140**, 4991–4994 (2018).
11. Wang, Y., Xu, J., Wang, Y. & Chen, H. Emerging chirality in nanoscience. *Chem. Soc. Rev.* **42**, 2930–2962 (2013).
12. Lee, H. E. et al. Amino-acid- and peptide-directed synthesis of chiral plasmonic gold nanoparticles. *Nature* **556**, 360–365 (2018).
13. Li, Y., Higaki, T., Du, X. & Jin, R. Chirality and surface bonding correlation in atomically precise metal nanoclusters. *Adv. Mater.* **32**, 1905488 (2020).
14. Chakraborty, I. & Pradeep, T. Atomically precise clusters of noble metals: emerging link between atoms and nanoparticles. *Chem. Rev.* **117**, 8208–8271 (2017).
15. Knoppe, S. & Bürgi, T. Chirality in thiolate-protected gold clusters. *Acc. Chem. Res.* **47**, 1318–1326 (2014).
16. Patty, J. B. et al. Crystal structure and optical properties of a chiral mixed thiolate/stibine-protected Au_{18} cluster. *J. Am. Chem. Soc.* **144**, 478–484 (2022).
17. Lopez-Acevedo, O., Tsunoyama, H., Tsukuda, T., Häkkinen, H. & Aikens, C. M. Chirality and electronic structure of the thiolate-protected Au_{38} nanocluster. *J. Am. Chem. Soc.* **132**, 8210–8218 (2010).
18. Li, Y. et al. Double-helical assembly of heterodimeric nanoclusters into supercrystals. *Nature* **594**, 380–384 (2021).
19. Huang, J.-H. et al. Symmetry breaking of atomically precise fullerene-like metal nanoclusters. *J. Am. Chem. Soc.* **143**, 12439–12444 (2021).

20. Knoppe, S., Dharmaratne, A. C., Schreiner, E., Dass, A. & Bürgi, T. Ligand exchange reactions on Au$_{38}$ and Au$_{40}$ clusters: a combined circular dichroism and mass spectrometry study. *J. Am. Chem. Soc.* **132**, 16783–16789 (2010).

21. Dolamic, I., Knoppe, S., Dass, A. & Bürgi, T. First enantioseparation and circular dichroism spectra of Au$_{38}$ clusters protected by achiral ligands. *Nat. Commun.* **3**, 798–804 (2012).

22. Knoppe, S., Dolamic, I., Dass, A. & Bürgi, T. Separation of enantiomers and CD spectra of Au$_{40}$(SCH$_2$CH$_2$Ph)$_{24}$: spectroscopic evidence for intrinsic chirality. *Angew. Chem. Int. Ed. Engl.* **51**, 7589–7591 (2012).

23. Zeng, C., Li, T., Das, A., Rosi, N. L. & Jin, R. Chiral structure of thiolate-protected 28-gold-atom nanocluster determined by X-ray crystallography. *J. Am. Chem. Soc.* **135**, 10011–10013 (2013).

24. Liu, X. et al. De novo design of Au$_{36}$(SR)$_{24}$ nanoclusters. *Nat. Commun.* **11**, 3349–3356 (2020).

25. Yan, J. et al. Asymmetric synthesis of chiral bimetallic [Ag$_{28}$Cu$_{12}$(SR)$_{24}$]$^{4-}$ nanoclusters via Ion pairing. *J. Am. Chem. Soc.* **138**, 12751–12754 (2016).

26. Deng, G., Teo, B. K. & Zheng, N. Assembly of chiral cluster-based metal-organic frameworks and the chirality memory effect during their disassembly. *J. Am. Chem. Soc.* **143**, 10214–10220 (2021).

27. Zhu, Y. et al. Enantioseparation of Au$_{20}$(PP$_3$)$_4$Cl$_4$ clusters with intrinsically chiral cores. *Angew. Chem. Int. Ed. Engl.* **57**, 9059–9063 (2018).

28. Knoppe, S. et al. Chiral phase transfer and enantioenrichment of thiolate-protected Au$_{102}$ clusters. *J. Am. Chem. Soc.* **136**, 4129–4132 (2014).

29. Yao, H. & Iwatsu, M. Water-soluble phosphine-protected Au$_{11}$ clusters: synthesis, electronic structure, and chiral phase transfer in a synergistic fashion. *Langmuir* **32**, 3284–3293 (2016).

30. Man, R. W. Y. et al. Synthesis and characterization of enantiopure chiral bis NHC-stabilized edge-shared Au$_{10}$ nanocluster with unique prolate shape. *J. Am. Chem. Soc.* **144**, 2056–2061 (2022).

31. Sugiuchi, M., Shichibu, Y. & Konishi, K. An inherently chiral Au$_{24}$ framework with double-helical hexagold strands. *Angew. Chem. Int. Ed. Engl.* **57**, 7855–7859 (2018).

32. Shen, H. et al. Tertiary chiral nanostructures from C-H···F directed assembly of chiroptical superatoms. *Angew. Chem. Int. Ed. Engl.* **60**, 22411–22416 (2021).

33. Wang, J.-Q., Guan, Z.-J., Liu, W.-D., Yang, Y. & Wang, Q.-M. Chiroptical activity enhancement via structural control: the chiral synthesis and reversible interconversion of two intrinsically chiral gold nanoclusters. *J. Am. Chem. Soc.* **141**, 2384–2390 (2019).

34. Zhang, M.-M. et al. Alkynyl-stabilized superatomic silver clusters showing circularly polarized luminescence. *J. Am. Chem. Soc.* **143**, 6048–6053 (2021).

35. Kong, Y.-J. et al. Photoresponsive propeller-like chiral AIE copper(I) clusters. *Angew. Chem. Int. Ed. Engl.* **59**, 5336–5340 (2020).

36. Yao, L.-Y., Lee, T. K.-M. & Yam, V. W.-W. Thermodynamic-driven self-assembly: heterochiral self-sorting and structural reconfiguration in gold(I)-sulfido cluster system. *J. Am. Chem. Soc.* **138**, 7260–7263 (2016).

37. Shi, L. et al. Self-assembly of chiral gold clusters into crystalline nanocubes of exceptional optical activity. *Angew. Chem. Int. Ed. Engl.* **56**, 15397–15401 (2017).

38. Knoppe, S., Dharmaratne, A. C., Schreiner, E., Dass, A. & Bürgi, T. Ligand exchange reactions on Au$_{38}$ and Au$_{40}$ clusters: a combined circular dichroism and mass spectrometry study. *J. Am. Chem. Soc.* **132**, 16783–16789 (2010).

39. Li, S. et al. Atom-precise modification of silver(I) thiolate cluster by shell ligand substitution: a new approach to generation of cluster functionality and chirality. *J. Am. Chem. Soc.* **140**, 594–597 (2018).

40. Huang, Y. & Hayashi, T. Chiral diene ligands in asymmetric catalysis. *Chem. Rev.* **122**, 14346–14404 (2022).

41. Trost, B. M. Asymmetric catalysis: an enabling science. *Proc. Natl Acad. Sci. USA* **101**, 5348–5355 (2004).

42. Li, M.-B., Wang, Y. & Tian, S.-K. Regioselective and stereospecific cross-coupling of primary allylic amines with boronic acids and boronates through palladium catalyzed C-N bond cleavage. *Angew. Chem. Int. Ed. Engl.* **51**, 2968–2971 (2012).

43. Li, M.-B. et al. Chemodivergent and diastereoselective synthesis of γ-lactones and γ-lactams: a heterogeneous palladium-catalyzed oxidative tandem process. *J. Am. Chem. Soc.* **140**, 14604–14608 (2018).

44. Li, M.-B. et al. Silver-triggered activity of a heterogeneous palladium catalyst in oxidative carbonylation reactions. *Angew. Chem. Int. Ed. Engl.* **59**, 10391–10395 (2020).

45. Li, M.-B. et al. Amino-supported palladium catalyst for chemo- and stereoselective domino reactions. *Angew. Chem. Int. Ed. Engl.* **60**, 670–674 (2021).

46. Fan, J.-Q., Yang, Y., Tao, C.-B. & Li, M.-B. Cadmium-doped and pincer ligand-modified gold nanocluster for catalytic KA^2 reaction. *Angew. Chem. Int. Ed. Engl.* **62**, e202215741 (2023).

47. Zhang, T.-S. et al. Open nitrogen site-induced kinetic resolution and catalysis of a gold nanocluster. *Nano Lett.* **23**, 235–242 (2023).

48. Li, M.-B., Tian, S.-K., Wu, Z. & Jin, R. Peeling the core-shell Au$_{25}$ nanocluster by reverse ligand-exchange. *Chem. Mater.* **28**, 1022–1025 (2016).

49. Yang, Y. et al. An efficient nanocluster catalyst for Sonogashira reaction. *J. Catal.* **401**, 206–213 (2021).

50. Das, A. et al. Nonsuperatomic [Au$_{23}$(SC$_6$H$_{11}$)$_{16}$]$^-$ nanocluster featuring bipyramidal Au$_{15}$ kernel and trimeric Au$_3$(SR)$_4$ motif. *J. Am. Chem. Soc.* **135**, 18264–18267 (2013).

51. Li, Q. et al. Molecular "surgery" on a 23-gold-atom nanoparticle. *Sci. Adv.* **3**, e1603193 (2017).

52. Li, Q. et al. Reconstructing the surface of gold nanoclusters by cadmium doping. *J. Am. Chem. Soc.* **139**, 17779–17782 (2017).

53. Li, Q. et al. A mono-cuboctahedral series of gold nanoclusters: photoluminescence origin, large enhancement, wide tunability, and structure-property correlation. *J. Am. Chem. Soc.* **141**, 5314–5325 (2019).

54. Teichert, J. F. & Feringa, B. L. Phosphoramidites: privileged ligands in asymmetric catalysis. *Angew. Chem. Int. Ed. Engl.* **49**, 2486–2528 (2010).

55. de Vries, A. H. M., Meetsma, A. & Feringa, B. L. Enantioselective conjugate addition of dialkylzinc reagents to cyclic and acyclic enones catalyzed by chiral copper complexes of new phosphorus amidites. *Angew. Chem. Int. Ed. Engl.* **35**, 2374–2376 (1996).

56. Alexakis, A., Vastra, J., Burton, J., Benhaim, C. & Mangeney, P. Asymmetric conjugate addition of diethyl zinc to enones with chiral phosphorus ligands derived from TADDOL. *Tetrahedron Lett.* **39**, 7869–7872 (1998).

57. Yan, X., Wang, Q., Chen, X. & Jiang, Y.-B. Supramolecular chiral aggregates exhibiting nonlinear CD-ee dependence. *Adv. Mater.* **32**, 1905667 (2020).

58. Chen, X.-X., Jiang, Y.-B. & Anslyn, E. V. A racemate-rules effect supramolecular polymer for ee determination of malic acid in the high ee region. *Chem. Commun.* **52**, 12669–12671 (2016).

Acknowledgements

Author contributions

M.-B.L. supervised the research and wrote the manuscript. M.-B.L. and S.Z. summarized the data. C.L., T.-S.Z. and C.-B.T. carried out the experiments. Y.Z. and W.F. resolved the structures of metal nanoclusters. All authors contributed to the preparation of the manuscript.

Competing interests

The authors declare no competing interests.

Additional information

Supplementary information The online version contains supplementary material available at
https://doi.org/10.1038/s41467-023-39462-w.

Correspondence and requests for materials should be addressed to Man-Bo Li.

Peer review information *Nature Communications* thanks Yunbao Jiang, and the other anonymous reviewer(s) for their contribution to the peer review of this work. A peer review file is available.

Reprints and permissions information is available at
http://www.nature.com/reprints

Publisher's note Springer Nature remains neutral with regard to jurisdictional claims in published maps and institutional affiliations.